Assessment of Techniques for Characterizing the Surface Quality of Ground Silicon Nitride

E.S. Zanoria, T.R. Watkins, K. Breder, L. Riester, M. Bashkansky, J. Reintjes, J.G. Sun, W.A. Ellingson, and P.J. Blau

(Submitted 29 September 1997; in revised form 16 March 1998)

This study evaluates techniques used to detect and quantify the extent of surface and subsurface damage in ground silicon nitride. Specimens of two differently ground surfaces of a hot isostatically pressed (HIP) silicon nitride, commercially designated as GS-44, were subjected to six types of analyses, namely mechanical stylus profiling, atomic force microscopy, point-counting analysis of fragmentation pits, laser-light scattering, optical gating, and grazing incidence x-ray diffraction (GIXD). The results of these investigations are compared and discussed. The techniques providing the clearest correlations with grinding conditions were mechanical stylus roughness, fragmentation analysis, and GIXD (residual stress conditions). Those that exhibited some correlation but appear to require more work to develop a reliable evaluation method were laser scattering and optical gating. Atomic force microscopy was useful, but not as a routine investigative tool for quality control in ceramic machining. The techniques that appear to have the most near-term potential for routine use are fragmentation analysis and optical gating. Laser-based optical scattering exhibits potential for routine application, but, more development is needed for its commercialization.

Keywords grinding, silicon nitride, surface characterization, surface wear

1. Introduction

Silicon nitride-based ceramics are finding increasing uses as structural and bearing materials. The preparation for most of these uses involves machining and final finishing operations. The cost-effective machining of ceramics presents special challenges over the machining of more widely used ferrous alloys. Material removal rates for ceramic machining are generally lower than those for metals, and more costly superabrasives like diamond must generally be used as well. New techniques, like high-speed grinding (Ref 1) and electrolytic in-process dressing (Ref 2), can help remove material faster, and improvements in processing have reduced the population of internal defects. However, the reduction of service life due to the existence of surface and near-surface, machining-induced flaws is still an issue. Because the fracture toughness of ceramics is typically less than that of metals, the need to reduce the number and sizes of flaws places special importance on developing improved quantitative methods for post-machining surface inspection.

The term *surface quality* means different things to different people. Sometimes, the term *quality* is related to cosmetic appearance, whereas at other times it might refer to the degree of smoothness or functionality. Thus, the measure of surface quality of a given part is logically application dependent. It is common to quantify surface quality in terms of the roughness parameters such as the arithmetic average roughness, root-mean-square roughness, and peak-to-valley roughness. With structural ceramics, one might also be concerned with the degree of porosity, amount of pull-out, or the presence of microfracture features on the finished surface. Another measure of surface quality is an indirect destructive one, namely the fracture strength of test bars whose tensile surface, in bending, is machined by the methods of current interest.

Although not without certain drawbacks, topographic assessment methods (stylus and non-contact profilometry) tend to dominate the field of surface quality assessment for ground ceramics. There are a variety of commercial instruments available to make such measurements, and industry has had a long-standing familiarity with the use of numerical roughness data. Yet, the roughness, waviness, and lay are but a small subset of a greater number of machined surface attributes, particularly those features that reside in machining-affected layers extending tens or even hundreds of micrometers deep. The methods for characterizing and quantifying the subsurface attributes of ground surfaces are in general more tedious to use, less numerically exact, and unfortunately often less repeatable. Brinksmeier (Ref 3) reviewed common nondestructive measuring techniques and discussed their usefulness for precision engineering applications. These techniques include grazing incidence x-ray diffraction, scanning acoustic microscopy, Raman spectroscopy, nano-indentation and photothermal microscopy.

The goal of this investigation was to explore the applicability of a wide range of both established and experimental methods to assess the quality of ground surfaces of silicon nitride. Issues of interest were simplicity of the methodology, suitability for use in routine production environments, type and repeatability of data, and degree of quantitativeness. This study required a team of investigators (the co-authors) who specialized in the application of a variety of techniques for ceramic surface characterization. The techniques fell into three broad

E.S. Zanoria, Oak Ridge National Laboratory, P.O. Box 2008, Oak Ridge, TN 37831-6063, USA (presently at Caterpillar Inc., PPG, Peoria, IL 61656-1895, USA); **T.R. Watkins, K. Breder, L. Riester,** and **P.J. Blau; M. Bashkansky,** and **J. Reintjes,** Naval Research Laboratory, Washington, DC 20375, USA; **J.G. Sun,** and **W.A. Ellingson,** Argonne National Laboratory, Argonne, IL 60439, USA.

categories: surface roughness and topographic measurement, subsurface microstructural characterization, and near-surface residual stress analysis. They were

- Mechanical stylus profilometry
- Atomic force microscopy (AFM)
- Point counting analysis of fragmentation pits
- Laser-based optical scattering detection
- Optical gating
- Grazing incidence x-ray diffraction (GIXD) analysis of residual stress

This study had intended to include micro-Raman analysis, but upon evaluation of preliminary results, it was determined that the technique was not sufficiently developed and quantitative to include in this comparison. Non-contact laser profilometry was also considered, but not included in this study because of inconsistencies in the preliminary set of data. This technique, which involves automated focusing of an infrared laser beam through a feedback focusing system, was used by Blau et al. (Ref 4) in a study to compare several methods of measuring the surface finish of ground ceramic and metal. Blau et al. suggested that the lower reflectivity of the ceramic surface could affect the ability of the laser to detect the sharpest focus point for the reflected beam. As a result, mechanical stylus data and AFM data did not agree with laser-based roughness data.

The GS-44 silicon nitride, an advanced ceramic of current interest for structural applications, was selected as specimen material and ground under two different sets of conditions to produce a considerable difference in the properties and characteristics of the test surfaces. To establish a link between the surface quality measures and functional performance, this study conducted sliding wear, repeated impact, and four-point bend tests on both types of ground GS-44.

2. Material and Methods of Grinding

The material used in this investigation was a hot isostatically pressed (HIP) silicon nitride (from Allied Signal, Ceramic Components Division, Torrance, CA, USA), designated as GS-44. This material was studied in detail in a collaborative project of the International Energy Agency (IEA) (Ref 5). According to the IEA, the mechanical behavior of GS-44 shows a systematic response to machining-induced damage. Typical properties of GS-44 are given in Table 1.

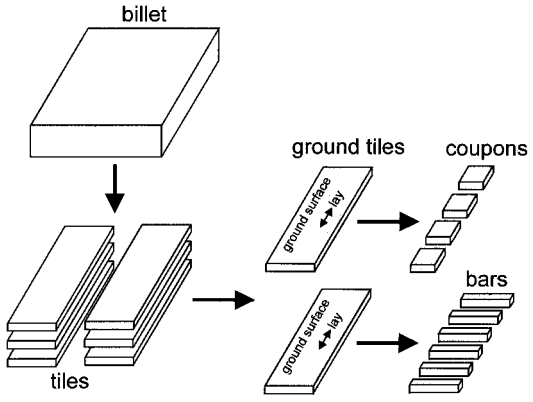

Fig. 1 Schematic of the preparation of the silicon nitride specimens. Ground coupons were used for surface characterization and surface durability tests; elongated bars were used for the four-point bend test.

The GS-44 was received originally as a hot isostatically pressed billet that was diced into rectangular tiles (130 × 45 × 6 mm) with a 0.8-mm thick diamond cut-off wheel (Fig. 1). Each tile was the stock material for grinding with the machining direction parallel to the sample length. The tiles were machined under two sets of conditions using a Harig CNC II surface grinder (Bridgeport Machine Tool Co., Bridgeport, CT). The two conditions differed primarily in the abrasive grit size of the 12.7-mm wide, resin-bonded diamond wheel. The condition categorized as "coarsely ground" used an 80-grit wheel (typical particle diameter, 177 μm) with an outer diameter of 152.4 mm. The other, regarded as "finely ground," used a 203.2-mm diameter wheel containing finer 320-grit (typical particle diameter, 44 μm) abrasives. The surface speeds of the wheels for the coarse and fine grinding were 35 and 47 m/s, respectively. Both speeds are typically used in machining practice. Machining for both conditions used a table speed of 200 mm/min, a 0.018-mm depth of cut, and a crossfeed of 1.8 mm with a water-based grinding fluid. After grinding, the tiles were each sliced into five square coupons (25.4 × 25.4 × 5.7 mm) with a 0.8-mm thick cut-off diamond wheel.

3. Surface Characterization Methods and Procedures

3.1 Surface Characterization

Mechanical Stylus Profilometry. The roughness of the ground surfaces was measured with a Talysurf 10 (TM) (Taylor Hobson Ltd., Leicester, England) surface profilometer. This system contains a position-sensitive opto-electrical transducer (pick-up) that registers vertical displacements of the stylus tip as it passes along the horizontal test surface. The diamond tip of the stylus has a penny-shaped or semicircular configuration with a radius of 2.5 μm. The degree to which the stylus faithfully replicates the surface topography is restricted by the size

Table 1 Physical and mechanical properties of test materials

	Silicon nitride	
Property	**GS-44(a)**	**NBD 200(b)**
Elastic modulus, GPa	310	320
Poisson's ratio (approx)	0.26	0.26
Surface finish	…	AFBMA grade 5 finish
Hardness, HV	15.5	16.6
Fracture toughness, MPa-m^2	8.6	4.1
Grindability(c), mm^3/N-m	8.9×10^{-4}	…

(a) Data from Allied Signal Ceramic Components, Torrence, CA, 1994. (b) Material used as the impacting body in repeated impact tests and also as a slider material for friction and wear tests. Data from Norton Advanced Ceramics, Worcester, MA. (c) Measured with the Ceramic Grindability Testing System with a motor-driven belt grinder and an automated loading system (described in Ref 6). The grinding conditions were normal load = 11.14 N; surface speed of grinding belt = 10.18 m/s; duration of grinding = 30s.

of the tip. Other factors being equal, a finer tip more faithfully replicates the roughness details.

The stylus is at one end of a pivoted beam that carries a slotted flag at the other end (Fig. 2). The flag is free to move between an illuminating system and a beam splitter. During a linear scan, the movement of the flag caused by the up-and-down motion of the stylus tip causes a departure from a null position and thus creates an imbalance in the electrical signals from the two photocells in the splitter. This difference, which has a magnitude proportional to the deflection of the beam, is converted to a modulated dc output. The system has a built-in datum for the relative displacement of the stylus. The pick-up signal is then processed by a desktop computer system with selectable filtration modes, cut-off lengths, number of cut-off, and roughness parameters.

A cut-off length (equivalent to the sampling length) is established to electronically suppress the lower frequencies of the waveform representing the waviness and the more widely spaced roughness irregularities. The product of the cut-off length and the number of cut-offs yields the evaluation length of the trace. In this study, seven cut-off lengths of 0.8 mm, which is within the recommended range (0.25 to 2.5 mm) for ground surfaces (Ref 7), were used. In practice, run-up and over-travel distances were added to the evaluation length so that the data were obtained at constant velocity. The traverse speed of the scan and the load applied by the stylus on the sample were preset by the manufacturer, respectively, at 0.5 mm/s and 1.00 mN.

The roughness parameters were determined based on pick-up signals that were electronically filtered by selecting the ASME (ISO) mode on the instrument. These parameters include the arithmetic roughness (R_a), root-mean-squared roughness (R_q), and maximum peak to valley height (R_t). The first two parameters were calculated from the equations:

$$R_a = (|y_1| + |y_2| \ldots + |y_n|)/n \quad \text{(Eq 1)}$$

$$R_q = [\,|(y_1^2| + |y_2^2| \ldots + |y_2^2|)/n\,]^{1/2} \quad \text{(Eq 2)}$$

where y_n is the absolute deviation from a center line, and n is the total number of data points.

Each GS-44 coupon was oriented such that the stylus moved perpendicular to the grinding-induced parallel grooves referred to as the lay. Measurements along a 5.6-mm evaluation length were made on nine locations distributed in a 3×3 arrangement. The midpoints of each evaluation length were 6 mm apart. For each location, the mean of three measurements was acquired.

Atomic Force Microscopy. The atomic force microscope used in this investigation (TopoMetrix, Santa Clara, CA, USA), has a pyramidal stylus attached to a flexible cantilever (Fig. 3). The stylus makes contact with the surface, and the repulsive force at the contact interface causes the cantilever to deflect away from the surface. The amount of deflection is monitored by a sensor consisting of a laser source that illuminated the tip of the cantilever and a mirror-photodetector array that detects the reflected light. Current signals from the sensor are transmitted to a feedback loop that maintains a constant cantilever deflection, hence a constant normal force. Cantilever deflection is maintained by adjusting the *z*-position of the stylus linked to a piezoelectric ceramic that is controlled by the feedback loop. The voltage required to adjust the piezoelectric ceramic is used as the *z*-data for topographic imaging.

The pyramidal stylus is made of silicon nitride and has a height and a base of 5 μm (aspect ratio of 1). According to the manufacturer, its tip radius is <50 nm. The stylus is mounted at the tip of a V-shaped, 1 μm thick cantilever. The cantilever, which is 200 μm long and 18 μm wide, has a spring constant of 0.064 N/m. In this study, a relative set-point current of 1 nA was applied to the feedback loop to maintain a constant force between the stylus and sample surface. For each specimen, a square of area 1×10^{-2} mm^2 was scanned in a raster mode at a rate of 200 μm/s. Each raster oriented perpendicular to the lay had a resolution of 400 pixels per line, and 400 lines were measured in the scanned area.

Point-Counting of Fragmentation Pits. Microscopic pits are formed in ceramic surfaces by fragmentation (pull-out) during grinding. The ground GS-44 specimens prepared for this study exhibited such features (Fig. 4). These pits have irregular shapes and varying sizes which can be as large as 6 μm across.

The relative proportion of fragmented areas on the surface is determined by manual point counting (Ref 1). The technique involves the superposition of a matrix of points on a scanning electron micrograph and counting the number of points that overlaid a fragmented area. A grid of 500 points (20×25 points) with 4-mm interval directions is generated through computer graphics software and then printed on a transparent cellulose film. The grid is overlaid on each micrograph for the point-counting procedure. A point located within the pit area has a count of 1, and a point lying on a pit boundary is counted as ½. The ratio of the number of counts for the pits to the total number of points in the matrix represents the fraction of area covered by the pits.

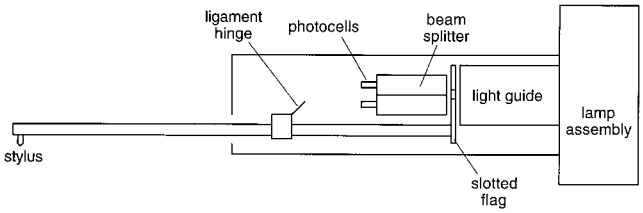

Fig. 2 Schematic of the mechanical stylus profilometer

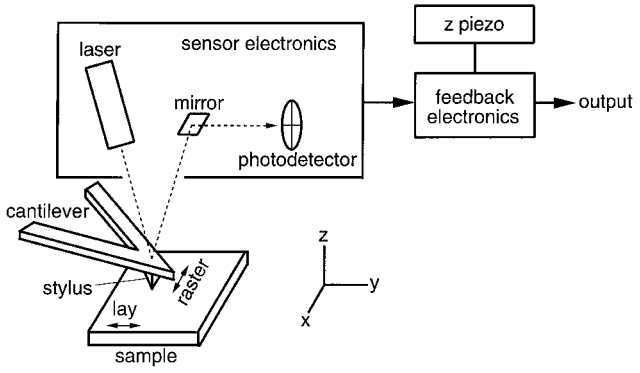

Fig. 3 Components of the atomic force microscope

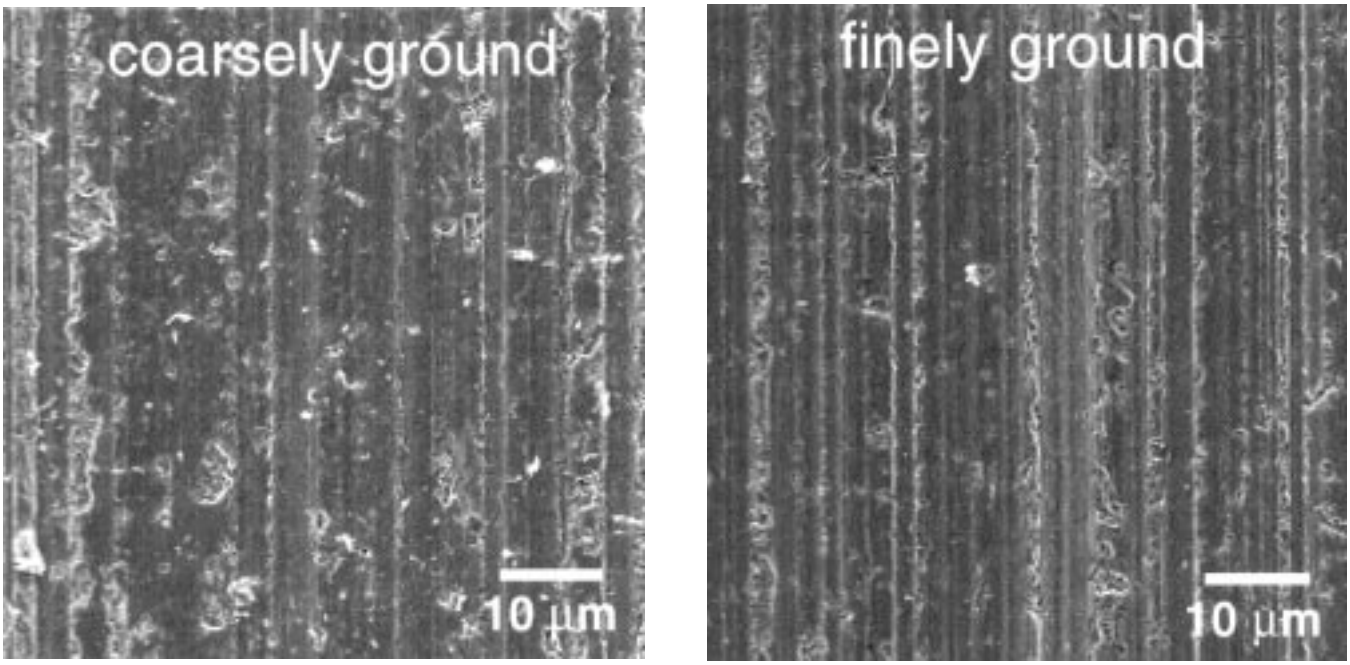

(a) **(b)**

Fig. 4 Scanning electron micrographs of coarsely and finely ground surfaces

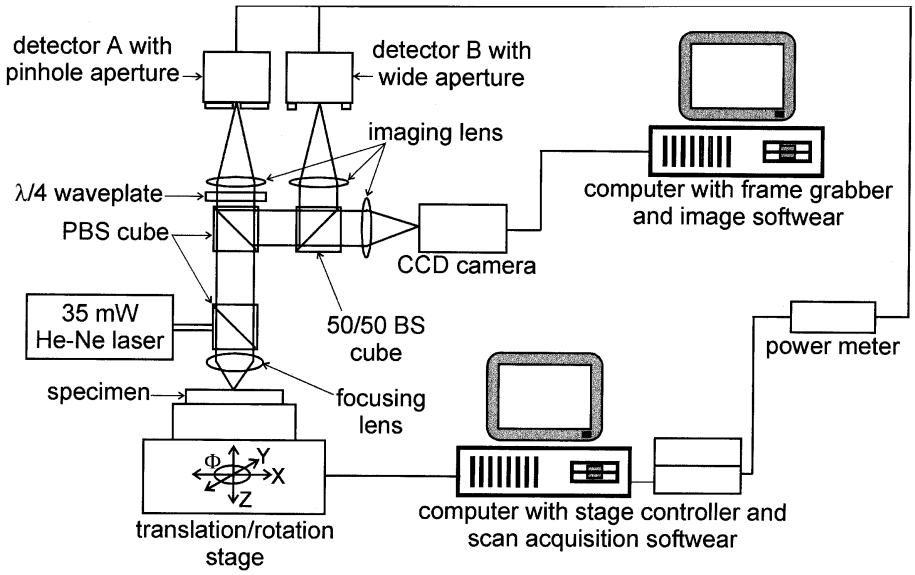

Fig. 5 Experimental setup used for laser-based optical scattering detection

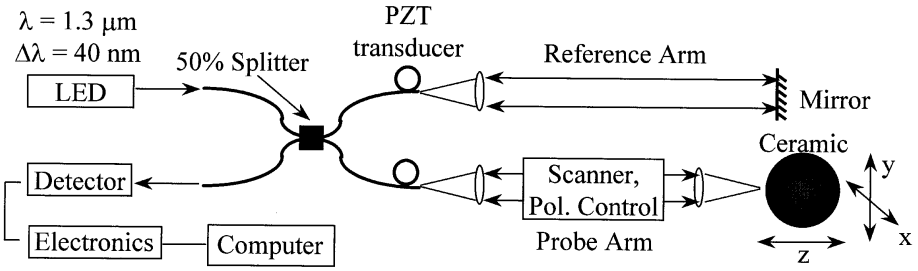

Fig. 6 Schematic of the low-coherence fiber interferometer system used for optical gating

This study used the Hitachi S-800 scanning electron microscope (Hitachi Ltd., Katsuta, Japan) at 5 kV to acquire images of the pull-out pits. For each ground GS-44 coupon, digitized scanning electron micrographs were taken at nine sampling locations. These locations were arranged in a 3×3 layout and had intervals of 3 mm along the *x* and *y* directions. Each micrograph was obtained at a magnification of 2000×. Point counting using the above configuration of the grid took about 9 min per micrograph.

Laser-based optical scattering detection is based on the fact that ceramics are translucent to infrared (IR) light. In several silicon nitride ceramics, the optical penetration depth is typically >100 μm (Ref 8). The transmitted beam is partially backscattered in the subsurface region by microstructural discontinuities such as cracks, crystallographic defects, and grain boundaries. In this regard, analysis of the backscattered light can be used to detect subsurface cracks formed by machining.

The experimental arrangement of the optical scattering system is shown in Fig. 5. A vertically polarized laser beam with a scanning resolution of 10 μm is directed through a polarizing beam-splitter (PBS) cube onto a horizontal sample surface. Light reflected from the surface would not undergo change in polarization unless the surface is extremely rough. Therefore, all surface-scattered light is reflected in the PBS and directed back toward the laser. The light scattered in the subsurface region underwent multiple reflections/refractions at grain boundaries and other microstructural discontinuities such that the polarization is altered. Consequently, randomized polarization is produced, creating a completely diffused backscatter. Half of this backscattered light is reflected into the PBS and directed back to the laser; the other half is transmitted through the same PBS. The transmitted light then passes through a second PBS. The optical signal is directed through a quarter-wave plate, imaged by a positive lens onto a polished stainless steel pinhole aperture (100 μm in diameter), and then recorded by Detector A. Only the subsurface-scattered light emanating from the incident spot (or central) region passes through the aperture and onto Detector A. The light scattered from the perimeter of the incident spot is reflected back through the lens and quarter-wave plate. This light, with a polarization rotated in the horizontal direction, is reflected into the second PBS and directed to a 50/50 beam splitter. One side of the 50/50 beam splitter is imaged by a positive lens onto Detector B, whereas the other side is imaged onto a charge coupled device (CCD) array to monitor the scattering surface.

The total backscattered intensity is measured by monitoring the sum of the outputs of detectors A and B (A + B). As the laser illumination is rastered across the specimen surface, the sum values are assembled into a gray-scale image of the surface, designated as the "sum" image. Application of the optical scattering technique to characterize a Vickers indentation in silicon nitride revealed that the sum image was strongly indicative of lateral cracks (Ref 8). The ratio of output B to output A (B/A) (ratio image) is sensitive to radial cracks around the indentation. Acquisition of 200×200 pixel ratio and sum images requires 50 s.

Optical gating also involves the analysis of backscattered light in the subsurface, but uses an ultrafast optical gate to detect the light scattered only from a particular depth. Optical gating suppresses the noise due to the light scattered inside the material and from the surface. The light reflected directly from a gated region travels a shorter path than the optical signals scattered from other depths. The latter signals arrive outside the gate at the detector and are consequently rejected. The gating technique used in the present study is based on optical coherence (Ref 9, 10). Previous studies (Ref 11-13) have established that optical gating techniques can be used to detect defects and imperfections on or below the surface of dense scattering materials such as ceramics or composites. The depth to which measurements can be done is determined by the sensitivity of the instrument and the degree of scatter and absorption in the sample.

The technique used in this work is based on a two-dimensional adaptation of an optical coherence domain reflectometer, shown schematically in Fig. 6. Incoherent light from a low-power, light-emitting diode (LED) is split in a fiber interferometer into two paths: reference and signal arms. The light in the reference arm is phase modulated by a piezoelectric transducer and reflected back from a mirror, while the light in the signal arm is focused on the sample surface. In a detector, the light scattered back from the sample interferes with the modulated light reflected from the reference mirror. The interference is detected only when both signals have the same path lengths within the coherence length of the light source. The length of the reference arm was adjusted to detect the light from the focal region in the signal arm. A two-dimensional image is acquired by scanning the optical beam along mutually perpendicular directions. These images are formed in a computer display by plotting the intensity of the light returned from a given point with respect to the scan position coordinates. The data from a single image is stored and displayed in logarithmic form to acquire signals with a wide range of intensities that could vary by several orders of magnitudes. This has been particularly useful for depth scans in highly scattering materials.

Images in the *X*-*Y* plane (parallel to the sample surface) and in the *X*-*Z* plane (perpendicular sample surface) were taken. Scans along the *X* direction were made with a fast galvanometer-controlled mirror. Motions along the *Y* and *Z* axes were done at speeds that allowed a time interval of less than 1 s for acquiring images with resolutions of 250×250 points.

The depth resolution of the device is determined by the coherence length of the light source, which is roughly proportional to its inverse bandwidth, whereas the lateral resolution is governed by the transverse dimension of the focal spot. This study used a 130-mW LED-producing light with a wavelength of 1.3 μm and a bandwidth of 40 nm. This provided a typical depth resolution in air of around 20 μm. The depth resolution inside the material is equal to the ratio of the depth resolution in air to the index of refraction in the solid (*N*). For silicon nitride, *N* is estimated to be 2.5 (Ref 10-12), which corresponded to a depth resolution of 8 μm. The light focused on the sample by a 4× microscope objective yielded a lateral resolution of about 10 μm.

Additionally, polarization control in the signal arm similar to the cross-polarization setup (e.g., in the laser-based optical scattering method) was applied to detect only the subsurface signal with a changed polarization state. This allowed the detection of birefringence occurring in the material and thus

reduction of the contribution of surface scattering to the total backscattered signal.

Grazing Incidence X-Ray Diffraction. Table 2 lists the details of the experimental conditions for the grazing incidence x-ray diffraction (GIXD) measurements. A four-axis goniometer

Table 2 Conditions used in grazing incidence x-ray diffraction (GIXD)

Parameter	Condition
Equipment	Scintag PTS goniometer MAC Science 18-kW rotating anode generator Scintag liquid N_2-cooled Ge detector
Power	10.5 kW; 35 kV, 300 mA
Radiation	CuKα_1, λ = 1.54059 Å
Incidence slit divergence	0.1°
Receiving slit acceptance	0.25°; radial divergence limiting (RDL) Soller slit
Source to specimen distance	360 mm
Specimen to back slit distance	280 mm
Tilt axis and angles	$\Omega = \alpha$; 0.4, 0.6, 1.0, 3.0, 7.0, 10.0°
Azimuthal axis and angles	ϕ; 0-360° in 30° steps (13 steps total)
Scans	0.02 °2Θ/step; 2-15 s/step; 140 < 2θ < 145°

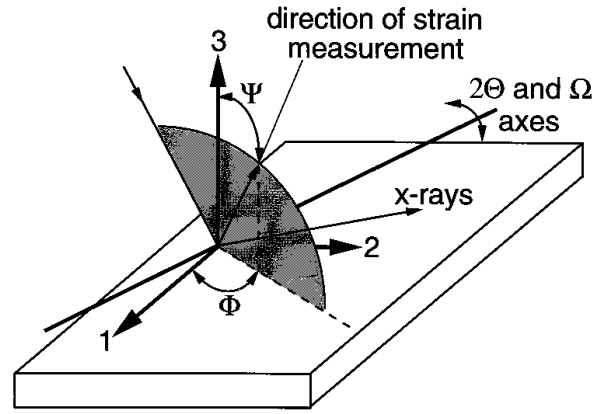

(a)

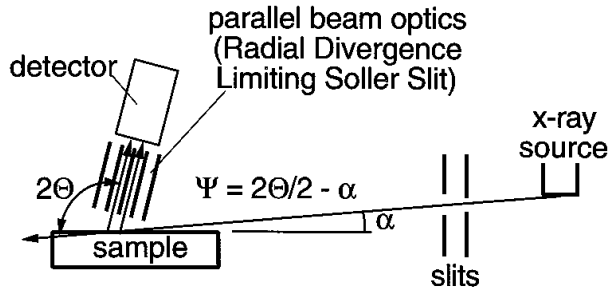

(b)

Fig. 7 Schematic representation of the grazing incidence x-ray diffraction (GIXD) method. (a) Definition of measurement axes with respect to the sample surface. The shaded region is the plane of diffraction containing the incident and diffracted x-rays, the surface normal and direction of strain measurement. The Ω axis is normal to the plane of diffraction (i.e., Ω is tilting). Note that Ω and α are equivalent for this work. (b) Schematic of GIXD experimental setup

(Ref 14) was used for the stress measurements using the Ω-goniometer geometry (Ref 15) (see Fig. 7a). The (323) reflection from the β-Si_3N_4 (141.3° 2θ) was used for the strain measurements in the samples. The 2θ scans were made as a function of the angle of incidence, α, and the azimuthal angle, ϕ. Figure 7(b) provides a schematic diagram of the GIXD experimental setup.

Goniometer alignment was ensured by examining LaB_6 powder on a zero background plate. The maximum observed peak shift for the (510) reflection of LaB_6 (141.7° 2θ) was less than 0.025° 2θ for Ω tilting, as described in Table 2. Sample alignment was accomplished using a dial gauge probe that was accurate to ± 5 μm. Here, the relative distance to the center of rotation is known, and the diffracting surface was positioned accordingly. First, an alignment block with a ~50-μm slit was mounted on the surface of the sample, which was offset such that the slit opening coincided with the center of rotation of the goniometer. Omega scans were performed for each pair of azimuthal angles (e.g., 0 and 180°) to determine the exact incidence angle where the beam passed through the slit, parallel to the sample surface. The incidence angles in Table 2 were adjusted correspondingly. Next, the sample surface was placed on the center of rotation using the dial gauge probe. Finally, a 325-mesh Ni powder was dispersed in acetone and painted onto the sample surface. Both the (331) reflection from the strain-free Ni (144.6° 2θ) and the (323) reflection from the β-Si_3N_4 were scanned as a function of angle of incidence. Figure 8 shows

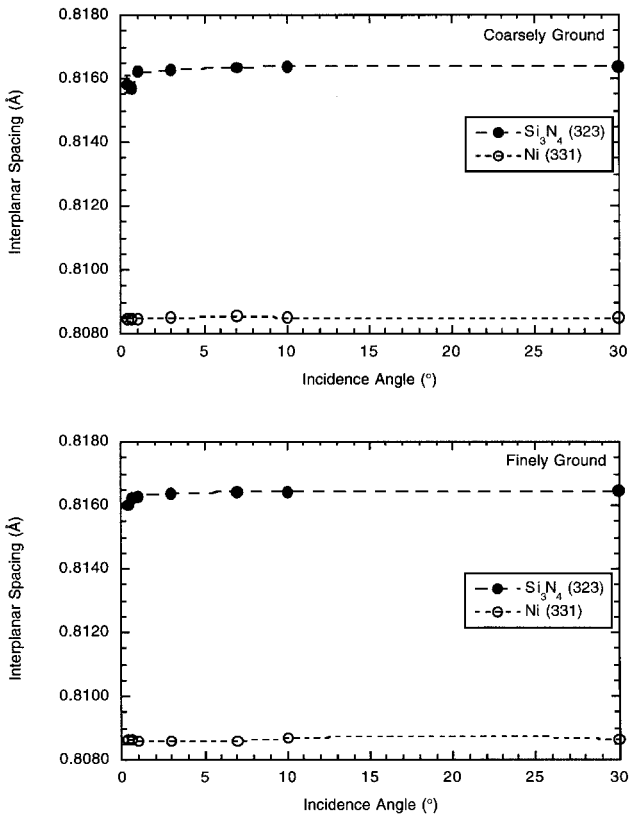

Fig. 8 Interplanar spacing plotted as a function of x-ray incidence angle

negligible change of the (331) Ni interplanar spacing as a function of incidence angle for the two samples examined. Thus, the changes observed in the (323) β-Si_3N_4 interplanar spacing originate from the sample and not from instrumental effects or sample displacement error.

The strain-free interplanar spacing, d_o, was calculated from measurements made at more conventional tilt angles using the Hauk method (Ref 16) and was taken as 0.8164 Å for the (323) reflection of β-Si_3N_4 for both samples. The $1/e$ (e = 2.718)) penetration depth, τ, was obtained according to the calculation of Ballard et al. (Ref 17). Furthermore, the data taken at $\alpha < 1°$ were corrected for refraction (Ref 17). The stresses were calculated using the method of Winholtz and Cohen (Ref 18) assuming a plane stress state (i.e., stresses σ_{13}, σ_{23}, and $\sigma_{33} = 0$). The Young's modulus and Poisson's ratio of β-Si_3N_4 were taken as 304 GPa and 0.26, respectively. Finally, estimates of the actual stress as a function of depth were made using the analysis method of Zhu et al. (Ref 19).

3.2 Durability Tests

Sliding Friction. The conditions for reciprocating sliding friction and wear tests, characterized by a ball-on-flat contact geometry, were those specified in Procedure A of ASTM Standard G-133-95 (Ref 20). These conditions are as follows:

- Normal force = 25 N
- Stroke length = 10.0 mm
- Reciprocating rate = 5 cycles/s
- Test duration = 10000 s (total sliding distance of 100 m)
- Atmosphere = room temperature air
- Relative humidity during testing = 40 to 60%

The tests were conducted on a Plint and Partners TE-77 (Plint and Partners, Ltd., Workingham, UK) machine that was calibrated with a load cell for normal force and a pulley and weight system for tangential (friction) force. The 9.52-mm diameter ball was made of hot isostatically pressed silicon nitride commercially designated as NBD-200 (Norton Advanced Ceramics, Worcester, MA). Table 1 shows the physical properties of the ball. Two directions of sliding were used, one parallel (longitudinal) and the other perpendicular (transverse) to the lay.

The grooves in the flat specimens were so deep such that the mechanical stylus instrument, normally used to measure wear, had insufficient range to make the measurement. Thus, a calibrated, noncontact Rodenstock laser profiling instrument (Optische Werke G. Rodenstock, Munich, Germany) was used instead. This offered the additional advantage of being able to map the topography of the scar. Cross-sectional areas of the wear groove were obtained at three places along the track, and their average was multiplied by the track length to obtain the wear volume, V_p, measured in cubic millimeters. Wear rate was calculated using the equation:

$$W_r = V_p/(P \cdot n) \quad \text{(Eq 3)}$$

where P is the normal force (N) and n is the number of sliding cycles. Because incremental data were not obtained, this calculation was based on the final wear volume and does not necessarily imply that the wear rate was constant throughout the experiment.

Repeated Impact. The repeated impact apparatus, which has a ball-on-flat contact geometry, was described in detail by Blau and Hanft (Ref 21). It has a cantilevered hammer that is pivoted at one end and periodically pushed by a motor-driven cam to move in an up-and-down motion. An NBD-200 ball (Table 1), attached to the moving end of the hammer, repeatedly struck the GS-44 coupon, which was mounted on an adjustable platform. In this study, the angle of incidence, which is the acute angle between the trajectory of impact and the sample surface, was varied. The conditions of the tests were

- Frequency = 3.33 Hz
- Velocity just before impact = 0.137 m/s
- Angles of incidence = 45 and 60°
- Duration of test = 10,000 impacts
- Peak incident force = 2.55 N
- Atmosphere = room temperature air

The coupon was oriented such that the tangential component of the impact force for oblique incidence was perpendicular to the lay. In each test, repeated impacts were interrupted at 1000, 2000, 3000, and 5000 cycles. During these periods, the contact surfaces were cleaned and the cross-sectional area of the crater was measured by mechanical stylus profilometry. Three tests were performed for each incident angle.

Flexural Strength. A four-point bend test was conducted to assess the role of machining-induced flaws on the flexure strength of the GS-44 silicon nitride. Procedure C of ASTM Standard C 1161-94 (Ref 22) was followed; however, two modifications were made in the test procedure. The above-mentioned grinding conditions were used instead of the ASTM procedure to prepare the surfaces of the test bars. Also, test bars were ground transversely, meaning that the lay was perpendicular to the bending-induced tensile stress. Such an orientation yields the highest sensitivity of the four-point bending test to the grinding-induced surface conditions.

For each grinding condition, 30 flexure bars with dimensions of $50 \times 4 \times 3$ mm were prepared (Fig. 1). One set of 20 bars was cut from the ground rectangular tile. The other ten bars were derived from one half of another ground tile. The second tile was ground separately, but under similar machining conditions. The fracture strength of the bars was then analyzed using Weibull statistics.

4. Results of Surface Characterizations

Repeated measurements of roughness parameters (R_a, R_q, and R_t) through mechanical stylus profilometry yielded standard deviations of less than 7% of their respective mean values. Table 3 shows a comparison of the roughness between the coarsely and finely ground coupons. Each data point is the average of nine sampling locations per specimen. The low standard deviations (3 to 7%) suggest that the surface roughness measured perpendicular to the lay was essentially uniform across the sample surface. The data reveal that the R_a, R_q, and R_t values of the finely ground surface were smaller than those of the coarsely ground surface by 30, 29, and 24%, respectively.

Figure 9 shows three-dimensional topographic plots of the ground surfaces acquired by atomic force microscopy. Each

plot is only a portion of the total scanned area. Table 3 provides the average roughness of three selected lines in the scanned area. The finely ground surface has R_a and R_t values that are smaller than those of the coarsely ground surface by 30 and 22%, respectively. Such differences in roughness are similar to those obtained by mechanical stylus profilometry. However, mechanical stylus profilometry yielded higher roughness values than those obtained by atomic force microscopy by a factor of 1.4 for R_a and 1.9 for R_t.

The average aerial fraction of fragmentation pits is 0.18 ± 0.05 for the coarsely ground and 0.07 ± 0.02 for the finely ground surface. There is a difference of 61%. Each of the aforementioned values represented an average of nine sampling points per specimen. Hence, the large standard deviations, ~28% of the average value, indicate a high degree of inhomogeneity in pit concentration across both ground surfaces.

Samples of elastic optical (laser) scattering images are shown in Fig. 10 for the coarsely and finely ground surfaces. These images were scanned perpendicular to the lay. Two distinguishing features are displayed by these images. One is the vertical lines that appear dark in the ratio image and lightly shaded in the sum image. These lines appear to coincide with the machining marks. The other feature is randomly distributed speckles, which are believed to emanate from isolated

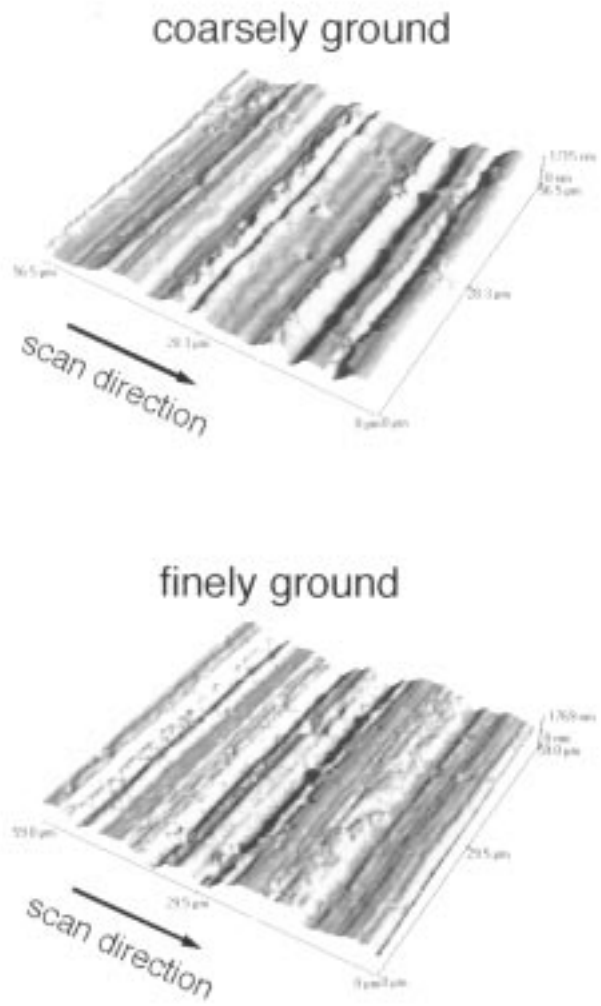

Fig. 9 Three-dimensional topographic images obtained using atomic force microscopy

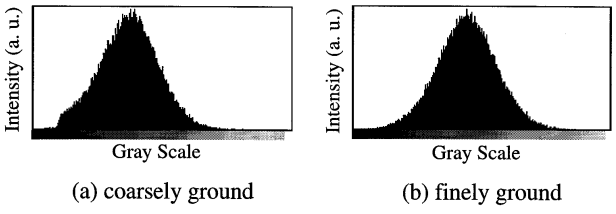

Fig. 11 Gray-scale histogram of the optical scattering ratio image. An arbitrary unit (a.u.) is used for the vertical axis of the histogram, which depends on the size of the image. The shape of the histogram reveals an intrinsic aspect of the image.

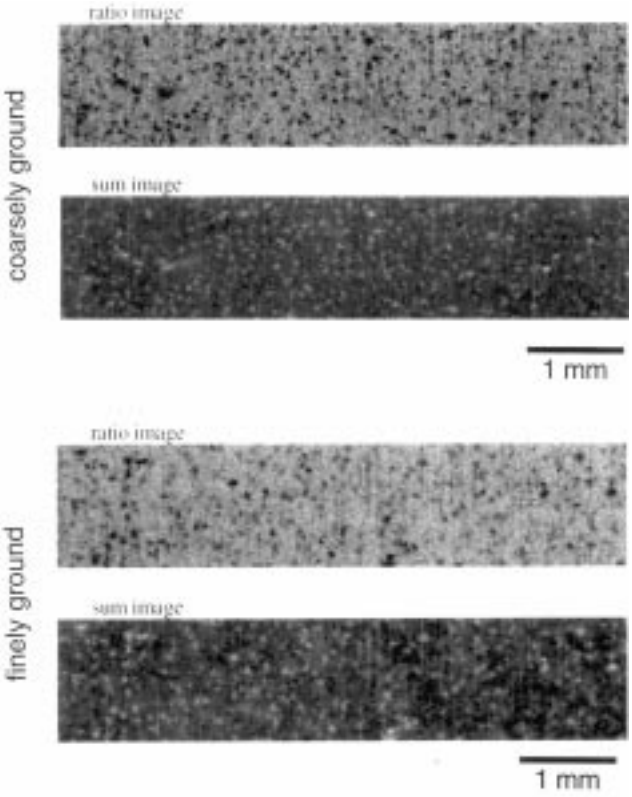

Fig. 10 Elastic optical scattering images of ground GS-44

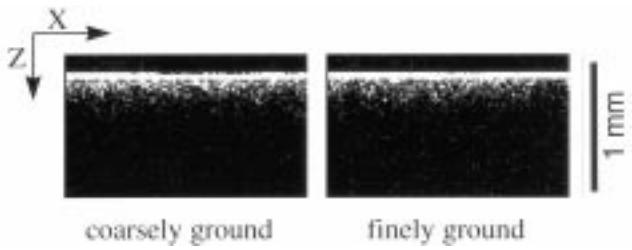

Fig. 12 Optically gated *X-Z* images of ground GS-44. Image plane is perpendicular to the surface.

damaged areas. A Fast Fourier Transform (FFT) analysis revealed that the dominant spatial period (inverse of frequency) of the speckles from the coarsely ground surface was 213 μm and that from the finely ground surface was 320 μm. The intensities of the scattering images in Fig. 10 can be represented by a gray-scale histogram. Histograms of the ratio images for coarsely ground surface are typically truncated at the low-gray region of the scale, as evidenced in Fig. 11(a). In contrast, the ratio-image histograms for the finely ground surface are relatively symmetrical (Fig. 11b). No distinction could be made between the coarsely and finely ground surfaces with respect to the pattern of sum-image histograms.

Figure 12 shows the optically gated images of the ground surfaces taken in the *X-Z* plane. With a graphics resolution of 250×125 points, each image represents a sample region that is 2 mm wide and 1 mm deep. The *X-Z* images reveal manifestation of defects as deep as 100 μm below the ground surface. These images, however, do not exhibit an apparent difference between the two ground surfaces. The *X-Y* images with a 2×2 mm area were acquired at depth increments of 2 μm. In Fig. 13, these images (250×250 points) are shown in pairs of coarsely and finely ground samples. Images of each pair for a given depth had their brightness adjusted by exactly the same factor so that they can be compared directly. Note, however, that the relative brightness cannot be used to compare *X-Y* images from different depths. Figure 13 shows that the parallel lines persist in images as deep as 8 μm, particularly in the coarsely ground GS-44. Images at 6 and 8-μm depths reveal two interesting features. One is the uneven intensity of the white lines across the scan area. Another is that these signals are stronger and extend

Table 3 Surface roughness data acquired with mechanical stylus profilometry and atomic force microscopy

Grinding conditions	Surface roughness, μm, obtained by: Mechanical stylus profilometry			Atomic force microscopy		
	R_a	R_q	R_t	R_a	R_q	R_t
Coarsely ground	0.53 ± 0.02	0.67 ± 0.01	4.10 ± 0.02	0.38 ± 0.02	…	1.99 ± 0.04
Finely ground	0.38 ± 0.02	0.48 ± 0.02	3.12 ± 0.02	0.27 ± 0.01	…	1.56 ± 0.06

Note: R_a = arithmetic roughness; R_q = root-mean-squared roughness; R_t = maximum peak-to-valley height

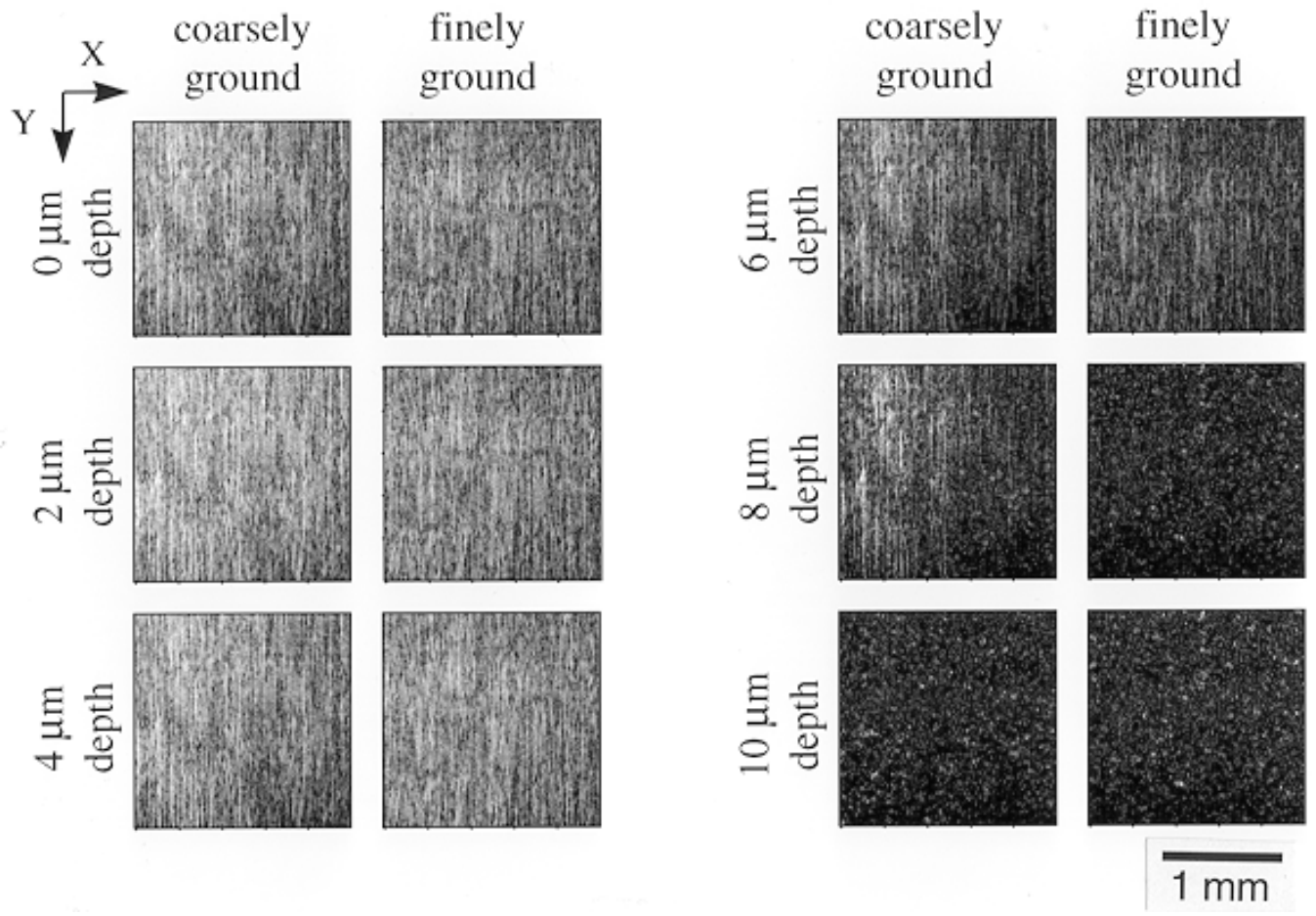

Fig. 13 Optically gated *X-Y* images of ground GS-44. Image plane is parallel to the surface.

deeper into the coarsely ground sample than into the finely ground GS-44 coupon. The *X*-*Y* scans of other locations of the ground samples also revealed the aforementioned observations at 6-m and 8-μm depths.

Figures 14 and 15 show the results of the GIXD analysis. The measured residual stress (open circles) for each x-ray penetration depth is designated as the tau (τ) profile. The *Z* profile (solid line) represents an estimate of the actual stress calculated as a function of depth and was deconvoluted from the tau profile using the analysis by Zhu et al. (Ref 19). It should be emphasized that the *Z*-profiles are estimates and are not unique for the data. The reconstructed tau profile (dotted line) was calculated from the solid line and is an estimate of the quality of the solid line. The fit of the reconstructed tau profile to the original tau profile is reasonable, thus indicating reliable *Z*-profile estimates.

The tau profiles show the residual stresses decaying rapidly with depth. As the depth of penetration increased, the x-ray penetration volume contained more of the material subjected to either tension or no stress. Thus, the average signal from such volume resulted in stresses that approached zero, which conformed with force balance constraints. Comparative data in Fig. 14 and 15 indicate that the residual stresses in the β-Si_3N_4 were greater in the coarsely ground sample than in the finely ground GS-44. For example, one can observe differences of 25 and 41% in the residual compressive stresses (from tau profile) at a 0.6-μm depth, oriented perpendicular and parallel to the lay, respectively. Moreover, the residual stresses perpendicular to the grinding direction were larger than those parallel to the lay. The *Z*-profiles in Fig. 14 and 15 show that the transition from compressive to tensile residual stress occur at depths between 0.5 and 2 μm. The finely ground coupon exhibits a shallower transition depth.

5. Results of Surface Durability Tests

Scanning electron microscopy of the deep grooves produced by the reciprocating sliding of the NBD-200 ball revealed that the original grinding marks had been completely obliterated (Fig. 16). Therefore, the effects of surface roughness were expected to be only temporary during the removal of the grinding marks (run-in process). The wear tracks exhibited long, shallow areas of granular appearance, indicative of wear by microfracture and surface fatigue. Such material removal processes would be expected in oscillating sliding. On the sides of the pitted areas were smooth deposits of adherent wear debris. Table 4 shows the wear rates of the ground coupons, indicating greater wear in the longitudinal than in the transverse sliding direction. These data also reveal that the material removal rate in the coarsely ground sample is lower than in the finely ground coupon by 17 and 13%, respectively, for the longitudinal and transverse sliding directions.

The change in the cross-sectional area of the impact crater with the number of impacts can be described by a power law

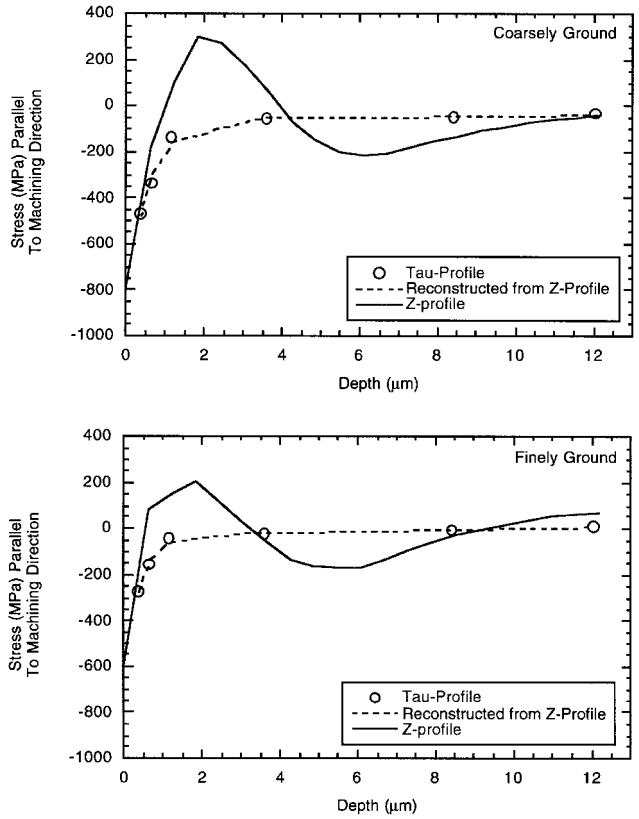

Fig. 14 Depth profile of residual stress parallel to the linear grinding grooves

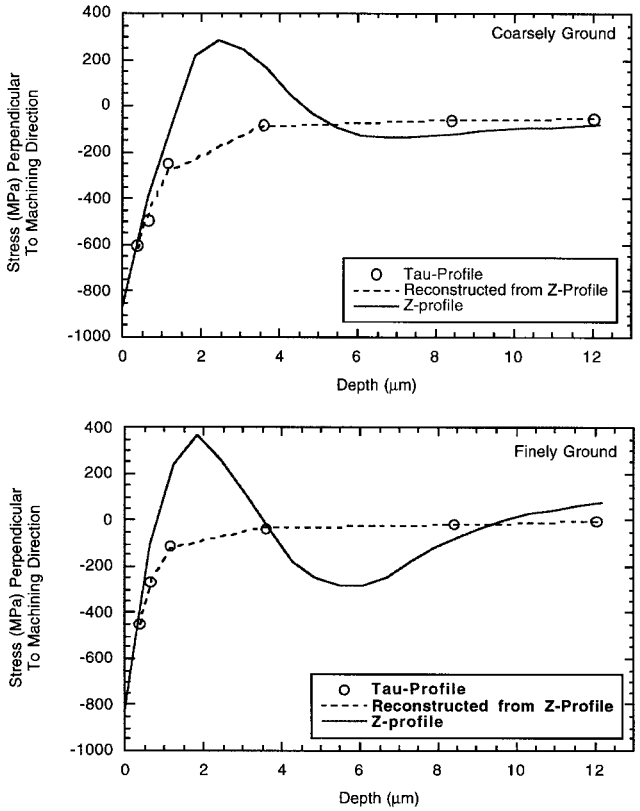

Fig. 15 Depth profile of residual stress perpendicular to the linear grinding grooves

curve, as shown in Fig. 17. This area is the average of two mutually perpendicular sections. Figure 17 indicates a lower rate of material removal in the coarsely ground sample than in the finely ground GS-44. At the early stage of crater evolution, damage to both of the ground surfaces was characterized by the lateral extrusion of slivers at the crests of elongated asperities (Fig. 18a), indicating plastic deformation. This process was accompanied by rapid oxidation of the slivers, as evidenced by surface chemical analysis of the debris, using energy-dispersive spectroscopy (EDS). This implies that the plastic deformation of elongated asperities is ensued by microfracture, thus producing a high ratio of surface area to volume in the impact-deformed layer. After a large number of impacts (>1000), flat surfaces consisting of truncated ridges developed at an increasing rate, and wear was dominated by the cyclic delamination of platelets made of compacted, crushed debris (Fig. 18b). The depths of the craters formed in the finely ground GS-44 after 10,000 impacts were higher than those in the coarsely ground sample by a factor of 1.1 to 1.2 (Table 4).

Four-point bending tests reveal that the average fracture strengths (30 bars per grinding condition) of the coarsely and finely ground GS-44 were 603 ± 51 and 900 ± 94 MPa, respectively (Table 5). As cited earlier, the total number of test bars per grinding condition was derived from two tiles that were machined separately. A difference in fracture strength between the tiles was noted. For the coarsely ground GS-44, the subset average strength was 571 and 668 MPa, whereas for the finely ground GS-44 774 and 963 MPa. The Weibull moduli of all the subsets were very high, ranging from 24 to 57. If the subsets per machining condition were combined, then Weibull moduli for both the coarsely and finely ground samples became approximately 12.

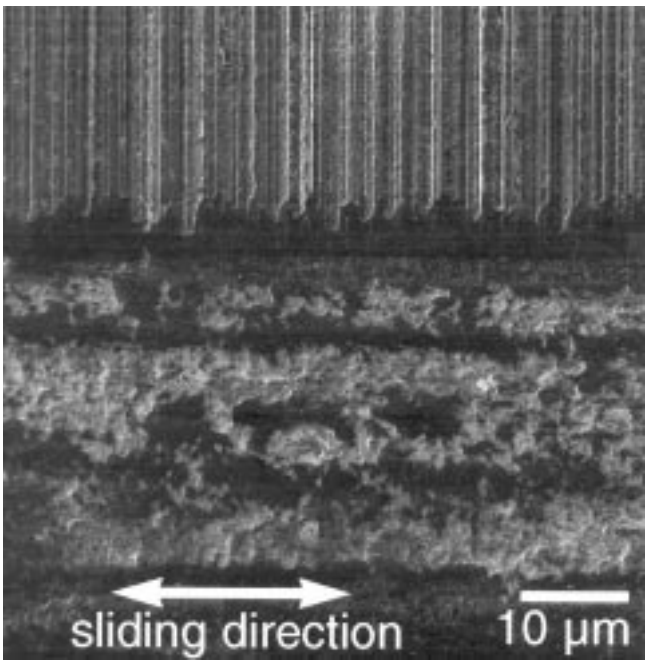

Fig. 16 Scanning electron micrograph of an edge of a sliding wear track in the GS-44 coupon. Grinding grooves are obliterated in the wear track due to a high wear rate.

Extensive fractography of the crack surfaces of the flexure specimens revealed that surface grinding produced flaws that control mechanical strength. However, the size and physical nature of these flaws were difficult to determine.

6. Discussion

Different means of characterizing the surface quality of a ground silicon nitride have been compared and evaluated. In this study, the term quality refers to three aspects: surface morphology, subsurface damage, and residual stress. Mechanical stylus profilometry, atomic force microscopy, and point-counting analysis of fragmentation pits were used to evaluate the surface morphology. Laser-based optical scattering and optical-gating techniques, both of which involve analysis of the behavior of transmitted light in a solid medium, were used to obtain information about subsurface damage. Measurement of subsurface residual stresses was obtained through GIXD. The

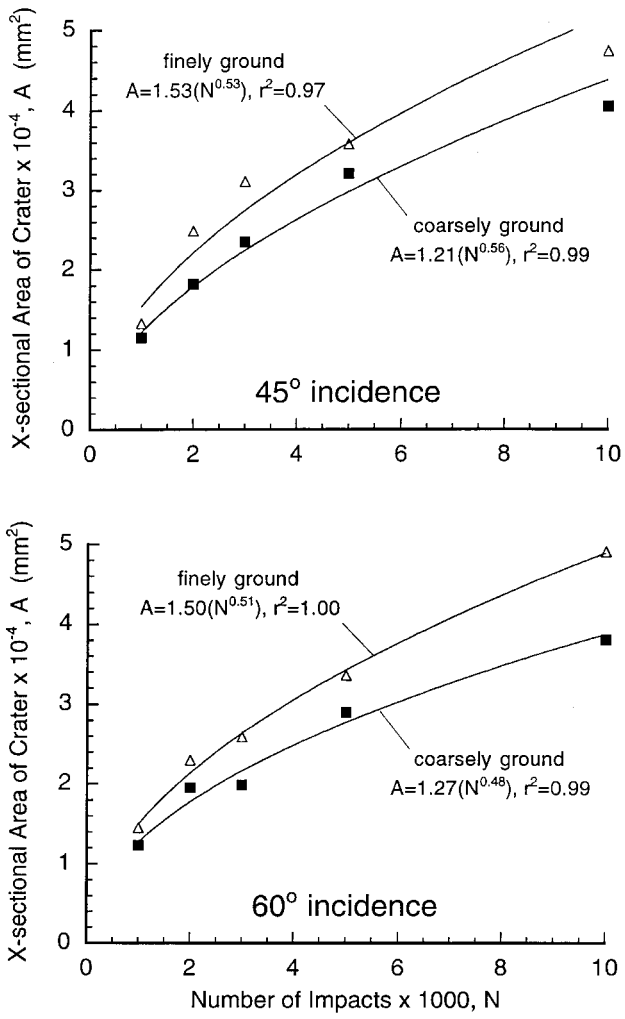

Fig. 17 Cross-sectional area of the crater plotted as a function of the number of impacts. The area that represents impact wear of the GS-44 coupon is an average of two mutually perpendicular sections of the crater.

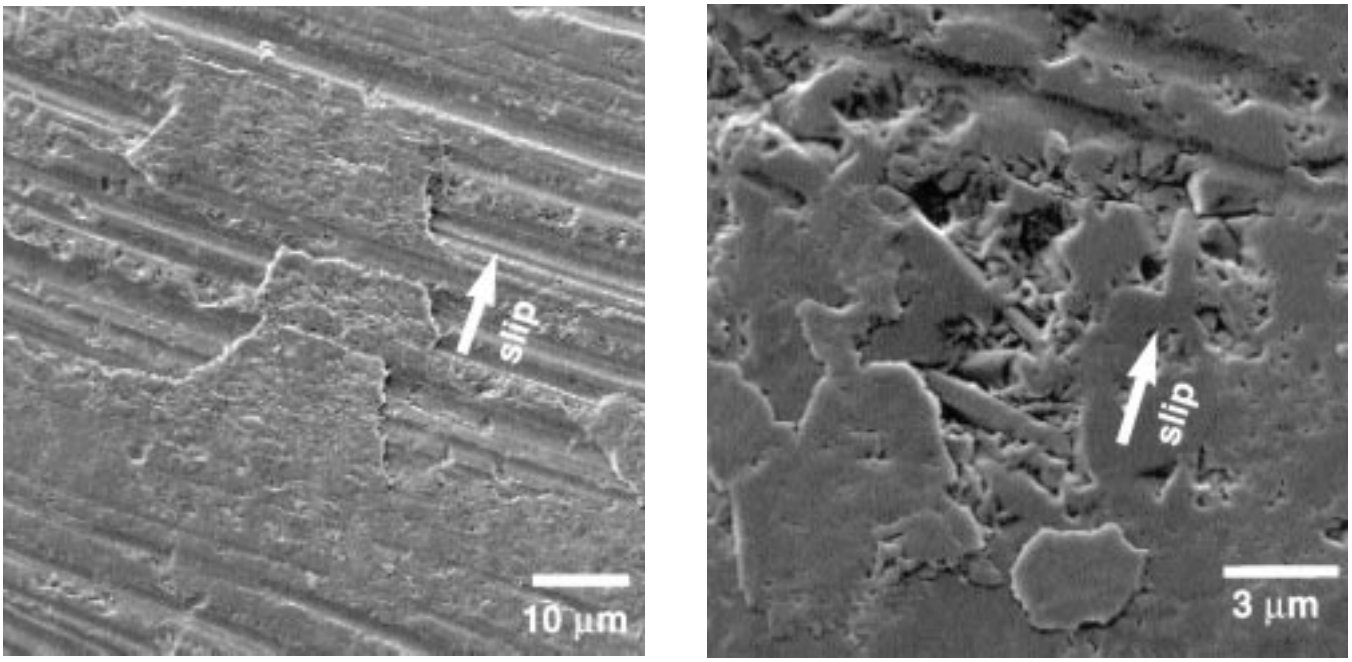

(a) (b)

Fig. 18 Scanning electron micrographs of repeated impact damge in ground GS-44. (a) Lateral extrusion of elongated ridges at 50 impacts. (b) Delamination of compacted, crushed debris at 10,000 impacts. Arrow indicates the direction of tangential slip during impact with oblique incidence.

Table 4 Surface wear of ground GS-44 coupons

Grinding conditions	Sliding wear rate $\times 10^{-4}$ (mm^3/N-cycle)		Depth of crater after 10,000 impacts, μm	
	Longitudinal(a)	Transverse(b)	45° incidence	60° incidence
Coarsely ground	1.41	1.08	1.55 ± 0.35	1.57 ± 0.08
Finely ground	1.70	1.24	1.71 ± 0.23	1.88 ± 0.14

(a) Sliding direction is parallel to the lay. (b) Sliding direction is perpendicular to the lay.

Table 5 Flexure strength of ground GS-44 silicon nitride

Grinding conditions	Average flexure strength(a), MPa	Unbiased characteristic strength(b), MPa	Unbiased weibull modulus
Coarsely ground	603 ± 51	626 (611,643)(c)	12.3 (9.6, 15.7)(c)
Finely ground	900 ± 94	959 (917, 968)(c)	12.3 (9.7, 15.8)(c)

(a) Each value is an average of 30 tests. (b) Calculated according to the Weibull theory using Maximum Likelihood Method. (c) Numbers in parentheses are upper and lower bounds.

relevance of these aspects of surface quality depends largely on the application of the machined component.

Some of the common engineering applications that were pertinent to the present study were tribological and/or structural in nature. Therefore, an important consideration in evaluating the usefulness of a surface characterization technique was its ability to predict precisely the functional performance of the component. A high degree of quantitativeness and repeatability of analytical results and a knowledge of how these results affect performance was required. From a manufacturing standpoint, however, one also has to consider the simplicity, speed, and suitability of the methodology for use in routine production settings.

Mechanical stylus profilometry exhibited excellent repeatability (standard deviation <7%) particularly for measurements made perpendicular to the lay. This technique, which can provide quantitative data, revealed a clear difference (~30%) in roughness (i.e., R_a, R_q, and R_t) between the coarsely and finely ground surfaces (Table 3). Atomic force microscopy can also produce quantitative results and exhibited nearly the same magnitude of difference in roughness between the two surfaces. However, the roughness values obtained through atomic force microscopy were lower than those acquired through mechanical stylus profilometry. For example, the maximum peak-to-valley height (R_t) of the coarsely ground surface was 1.99 μm as measured by the former, whereas the latter method yielded 4.10 μm. Such a discrepancy, also observed by Blau et al. (Ref 4), is inconsistent with fact that the stylus tip radius

used in the AFM (<0.05 μm) was much smaller than the one used for mechanical stylus profilometry (2.5 μm). The stylus with the finer tip, which in principle can penetrate into deep valleys, was expected to more faithfully replicate the surface roughness. One possible explanation was that the internal calibrations of one of the instruments were in error. However, the present study found no significant error in instrument calibration using reference grids. Another possibility was that the pyramidal silicon nitride stylus used in the atomic force microscopy procedure was worn during the raster. In fact, Khurshudov et al. (Ref 23) reported a noticeable wear of a three-sided pyramidal diamond tip of an AFM after several cycles of linear scratches against a single-crystal silicon under a normal load of 60 μN. However, the present study produced no direct evidence of stylus wear. The authors could find no other plausible explanation for this discrepancy in the results without access to the software used to process the data.

A different approach for describing surface morphology, the point-counting method, has been demonstrated to be an excellent means of quantitatively contrasting the concentration of fragmentation pits on the two ground GS-44 surfaces. In fact, the difference in pit concentration between the two surfaces was hardly noticeable through mere visual inspection of the micrographs. One should note that the point-counting method requires consistency in visual identification of the pits and their boundaries. The high standard deviation of the average pit concentration (0.18 ± 0.05 for coarsely ground and 0.07 ± 0.02 for finely ground) indicated spatial variability in surface condition and suggests that making point-counts on several locations on the surface is necessary to acquire a representative average value.

Surface profilometry and point-counting analysis produce data that directly quantify a surface condition. In contrast, techniques involving analysis of the scattering of incident electromagnetic radiation (e.g., light or x-rays) provide data that only indirectly represent subsurface conditions. The laser-based optical scattering technique revealed a large difference in the dominant spatial periods of speckles in B/A ratio images taken perpendicular to the lay. Assuming isotropic distribution of the speckles, these periods could be linked to the machining marks. Moreover, the truncation of the gray-scale histogram (of ratio image) for the coarsely ground surface at the low-gray region (Fig. 11a) is indicative of a strong defect pattern that is most likely associated with the grinding marks. Although the optical-scattering technique succeeded in distinguishing the two grinding conditions, more study is needed to quantitatively correlate the backscattering signatures with flaw size distribution and depth of the subsurface damage zone.

The optical-gating technique showed potential for acquiring quantitative data about the depth of machining-induced damage because of its ability to select signals from specific depths. Optical-gating images (Fig. 13) reveal the persistence of white parallel lines in the coarsely ground sample and the disappearance of these features in the finely ground GS-44 at depths 8 μm below the surface. This depth is greater than the maximum peak-to-valley heights (3.1 and 4.1 μm), as measured by mechanical stylus profilometry, and tends to rule out the possibility that the lines were caused by topography alone. It is also possible that the white lines, which are parallel to the lay, correspond to cracks with planes perpendicular to the surface and parallel to the grinding direction. However, such cracks that break through the surface were not observed by either atomic force (Fig. 9) or scanning electron microscopy (Fig. 4). The white lines in Fig. 13 could also be representations of narrow plastically deformed zones underneath the abrasion grooves (Ref 24). Improving the depth resolution by at least a factor of three through modification of the optical-gating apparatus could help resolve the physical nature of the white lines.

Grazing incidence x-ray diffraction results showed that the coarsely ground surface had a higher residual compressive stress than the finely ground surface. This observation agrees with that of van den Berg and de With (Ref 25) who measured the residual stress of ground magnesium–partially stabilized zirconia using a different x-ray diffraction method. Eigenmann and Macherauch (Ref 26) reported residual compressive stress gradients in ground Al_2O_3 and ZrO_2 similar to those shown in Fig. 14 and 15. The depths at which the compressive stresses became zero in the aforementioned ceramics are comparable to those observed in this study. These authors also found that the residual compressive stresses transverse to the lay were higher than those that were parallel. The agreement of the residual stress data in this study with those of previous work indicates the reliability of the x-ray diffraction method in characterizing subsurface conditions of ground surfaces. However, this technique samples only localized regions of a surface. Thus, multiple measurement sites are necessary to account for any heterogeneities in residual stress distribution; however, the data for each site takes hours to obtain.

Among all the surface analytical results in this study, those obtained by GIXD best explain the results of sliding friction (Table 4) and repeated impact tests (Fig. 17). As discussed earlier, wear of the ground surfaces in these tests largely involves microfracture. The low wear sustained by the coarsely ground surface is attributed to its higher residual compressive stress, which impedes the rate of microcrack propagation.

Despite having a higher surface concentration of pull-out pits, the coarsely ground GS-44 coupon still exhibits a lower rate of repeated impact and sliding wear. In this regard, the pull-out pits appear to be very shallow machining-induced flaws, apparently without influence on the subsurface strength of the ground material. However, the residual compressive stress gradients in the subsurface regions exert a strong effect on the propagation of microcracks initiated by either impact or reciprocating sliding. In fact, the impact crater depths (1.5 to 2 μm) produced in the ground samples after 10,000 impacts were within range of the depths at which transitions from compressive to null residual stress occurred (refer to the tau profiles in Fig. 14 and 15). The coarsely ground surface, which exhibits a deeper transition, has more residual compressive stress and hence higher resistance to microfracture in the near-surface regions. Using GIXD, Pfeiffer and Hollstein (Ref 27) observed an increase in the depth of residual compressive stress in ground silicon nitride with larger abrasive grit size.

Although the coarsely ground GS-44 was more durable under repeated impact or reciprocating sliding conditions, it exhibited a lower flexure strength than that of the finely ground sample (Table 5). The high residual compressive stress in the coarsely ground specimen should theoretically provide a

Table 6 Summary evaluation of surface characterization methods

Technique	Time to acquire data	Degree of repeatability	Type of data	Remarks
Mechanical stylus profilometry	~ 11 s/line scan	Very high (across the lay)	Roughness values; topographic image	Distinguishes machined surface conditions; no indication of stress or subsurface flaws
Atomic force microscopy	3 – 4 min/area scan	Moderate (across the lay)	Roughness values; topographic image	Distinguishes machined surface conditions; no indication of stress or subsurface flaws
Non contact laser profilometry	~ 11 s/line scan	…	Roughness values; topographic image	Results on ceramic surfaces are questionable; do not agree with other methods
Point-counting analysis of fragmentation pits	~ 9 min/micrograph	Moderate	Surface concentration of pits	Distinguishes machined surface conditions; spatial variation of pit concentration indicates the uniformity of machined surface condition
Laser-based optical scattering detection	50 s/area scan	…	Light-scattering images; gray-scale histograms; FFT(a)	Distinguishes machined surface conditions; gives qualitative description of flaws; promising technique; requires more development work
Optical-gating technique	< 1 s/two-dimensional image	High	Depth of subsurface structures	Promising technique to quantify depth and size of flaws; requires more development work
Grazing incidence x-ray diffraction	48 h sample	High	Residual stress-depth profile	Distinguishes machined surface conditions; data are useful for surface wear analysis

(a) Fast fourier transform

higher resistance to bending. It should be noted, however, that failure of a ceramic originates at the largest flaw subjected to tension. Thus, the flexure strength of the ground GS-44 is not an averaged effect of the flaw population nor is it governed by a typical flaw size. It is linked to the worst machining-induced flaw that experiences maximum tensile stress. In this regard, the possibility that such a flaw could occur in tensile regions below the topmost layer with the residual compressive stress (see *Z*-profiles in Fig. 14 and 15) could not be ruled out. The gray-scale histograms of B/A ratio images (Fig. 11), which are sensitive to median cracks perpendicular to the surface, and the optically gated *X*-*Y* images (Fig. 13) seem to indicate a greater degree of machining-induced subsurface damage in the coarsely ground GS-44. Unfortunately, these data lack quantitative information about the size and location of the subsurface flaws.

7. Conclusions

An evaluation of the various surface characterization techniques used in this study is summarized in Table 6. The conclusions of this study are as follows. Mechanical stylus profilometry and atomic force microscopy yield similar differences in the roughness between the coarsely and finely ground surfaces. For a given surface condition, the former produced higher numerical roughness values.

Point-counting analysis is a simple technique that quantifies surface concentration of pull-out pits. Several sampling points are necessary to acquire a representative surface concentration because the pits are not uniformly distributed, particularly in coarsely ground surfaces. The laser-based optical scattering detection yields quantitative differences between the coarsely and finely ground surfaces with respect to the intensity and frequency of backscattered light. The correlation between backscattered images and subsurface structures is not yet clearly established and needs more development.

The optical-gating technique can qualitatively detect the depth of subsurface features associated with grinding. The resolution of the present optically gated images needs further enhancement to identify and measure the size of subsurface microstructures. Grazing incidence x-ray diffraction provides quantitative residual stress data that are useful in analyzing differences in the wear behavior of a ground ceramic surface.

The flexure strength of ground silicon nitride is controlled by the largest flaw produced by surface grinding. The weaker material is associated with a rougher surface. However, finding the critical flaw where failure initiates is not yet possible. Improvements in optical scattering detection or the optical-gating technique could help resolve this issue.

Acknowledgments

The authors acknowledge the support of the U.S. Department of Energy, Assistant Secretary for Energy Efficiency and

Renewable Energy, Office of Transportation Technologies, as part of the Propulsion System Materials Program, under contract DE-AC05-96OR22464 with Lockheed Martin Energy Research Corp. In addition, this research was supported in part by an appointment of E.S. Zanoria to the Oak Ridge National Laboratory Postdoctoral Research Associates Program administered jointly by Oak Ridge National Laboratory (ORNL) and the Oak Ridge Institute for Science and Education (ORISE). Grinding and cutting of the GS-44 billets into test coupons were performed by the ORNL Machining and Inspection Research Group.

References

1. J.A. Kovach, P.J. Blau, S. Malkin, S. Srinivasan, B. Bandyopadhyay, and K. Ziegler, A Feasibility Investigation of High Speed, Low Damage Grinding for Advanced Ceramics, *Proc. of the 5th Int. Grinding Conf.*, MR93-352, Society of Manufacturing Engineers, 1993, p 1-16
2. B.P. Bandyopadhyay, "Application of Electrolytic In-Process Dressing for High-Efficiency Grinding of Ceramic Parts," Oak Ridge National Laboratory Special Report ORNL/SUB/96-SV716/1, Oak Ridge, TN, 1997
3. E. Brinksmeier, State-of-the-Art of Non-Destructive Measurement of Sub-Surface Material Properties and Damages, *Precis. Eng.*, Vol 1 (No. 4), 1989, p 211-224
4. P.J. Blau, R.L. Martin, and L. Riester, "A Comparison of Several Surface Finish Measurement Methods as Applied to Ground Ceramic and Metal Surfaces," Oak Ridge National Laboratory Special Report ORNL/M-4924, Oak Ridge, TN, 1996
5. K. Breder and M.K. Ferber, "Effect of Machining Conditions on the Strength of Silicon Nitride—Results From Research Performed in the United States, International Energy Agency—Annex II, Co-Operative Program on Ceramics for Advanced Engines and Other Conservation Applications," Oak Ridge National Laboratory, Oak Ridge, TN, 1996
6. C. Guo and R.H. Chand, "Cost-Effective Method For Determining the Grindability of Ceramics," Oak Ridge National Laboratory Special Report ORNL/SUB/93-SM036/1, Oak Ridge, TN, 1997
7. H. Dagnall, *Exploring Surface Texture*, 2nd ed., Rank Taylor Hobson Limited, Leicester, England, 1986, p 81-83
8. J.G. Sun, M. Shirber, and W.A. Elingson, Laser-Based Optical Scattering Detection of Surface and Subsurface Defects in Machined Si_3N_4 Components, *Ceramic Engineering and Science Proc.*, Vol 18 (No. 4), J.P. Singh, Ed., The American Ceramic Society, OH, 1997, p 273-280
9. R.C. Youngquist, S. Carr, and D.E.N. Davies, "Optical Coherence-Domain Reflectometry: A New Optical Evaluation Technique," *Opti. Lett.*, Vol 12 (No. 3), 1987, p 158-160
10. K. Takada, I. Yokohama, K. Chida, and J. Noda, New Measurement System for Fault Location in Optical Waveguide Devices Based on an Interferometric Technique, *Appl. Opt.*, Vol 26 (No. 9), 1987, p 1603-1606
11. P.R. Battle, M. Bashkansky, R. Mahon, and J. Reintjes, Subsurface Defect Detection in Ceramic Materials Using Optical Gating Techniques, *Opt. Eng.*, Vol 35 (No. 4), 1996, p 1119-1123
12. M. Bashkansky, P.R. Battle, M.D. Duncan, M. Kahn, and J. Reintjes, Subsurface Defect Detection in Ceramics Using an Optical Gated Scatter Reflectometer, *J. Am. Ceram. Soc.*, Vol 79 (No. 5), 1996, p 1397-1400
13. M. Bashkansky, M.D. Duncan, M. Kahn, D. Lewis III, and J. Reintjes, Subsurface Defect Detection in Ceramics by High-Speed High-Resolution Optical Coherent Tomography, *Opti. Lett.*, Vol 22 (No. 1), 1997, p 61-63
14. H. Krause and A. Haase, X-Ray Diffraction System PTS for Powder, Texture, and Stress Analysis, *Experimental Techniques of Texture Analysis*, H. J. Bunge, Ed., DGM Informationsgesellschaft, Verlag, Oberursel, 1986, p 405-408
15. I.C. Noyan, and J.B. Cohen, *Residual Stress, Measurement by Diffraction and Interpretation*, Springer-Verlag, 1987, p 101
16. I.C. Noyan, and J.B. Cohen, *Residual Stress, Measurement by Diffraction and Interpretation*, Springer-Verlag, 1987, p 129-130
17. B. Ballard, X. Zhu, P. Predecki, and D. Braski, Depth-Profiling of Residual Stresses by Asymmetric Grazing Incidence X-Ray Diffraction (GIXD), *Proc. of Fourth Int. Conf. on Residual Stresses*, Society for Experimental Mechanics, 1994, p 1133-1143
18. R.A. Winholtz and J.B. Cohen, Generalized Least-Squares Determination of Triaxial Stress States by X-Ray Diffraction and the Associated Errors, *Aust. J. Appl. Phys.*, Vol 41 (No. 2), 1988, p 189-199
19. X. Zhu, B. Ballard, and P. Predecki, Determination of Z-Profiles of Diffraction Data from τ-Profiles using a Numerical Linear Inversion Method, *Advance X-Ray Analysis*, Vol 38, Plenum Press, 1995
20. "Standard Test Method for Linearly Reciprocating Ball-on-Flat Sliding Wear," ASTM Standard G 133-95, *Annual Book of Standards*, Section 3, Vol 03.02, American Society for Testing and Materials, 1996, p 521-528
21. P.J. Blau and T.A. Hanft, Quantitative Measurement of Repetitive Impact Damage on Ground Silicon Nitride Surfaces, *Tribol. Int.*, Vol 27 (No. 2), 1994, p 109-118
22. "Standard Test Method for Flexural Strength of Advanced Ceramics at Ambient Temperature," ASTM Standard C 1161-94, *Annual Book of Standards*, Section 15, Vol 15.01, American Society for Testing and Materials, 1996, p 306-310
23. A.G. Khursuhdov, H. Kato, and H. Koide, Wear of the AFM Diamond Tip Sliding Against Silicon, *Proc. of the 11th Int. Conf. on Wear of Materials*, D. Rigney and R.G. Bayer, Ed., Elsevier, 1997, p 22-27
24. H.P. Kirchner, Damage Penetration at Elongated Machining Grooves in Hot-pressed Si_3N_4, *J. Am. Ceram. Soc.*, Vol 67 (No. 2), 1984, p 127-132
25. P.H.J. van den Berg and G. de With, Strength and Residual Stress of Mg-PSZ after Grinding, *Wear*, Vol 160 (No. 2), 1993, p 301-308
26. B. Eigenmann and E. Macherauch, Determination of Inhomogeneous Residual Stress States in Surface Layers of Machined Engineering Ceramics by Synchrotron X-Rays, *Nucl. Instrum. Methods Phys. Res. B*, Vol 97, 1995, p 92-97
27. B.W. Pfeiffer and T. Hollstein, Damage Determination and Strength Prediction of Machined Ceramics by X-Ray Diffraction Techniques, *Machining of Advanced Materials*, NIST Special Publication 847, S. Jahanmir, Ed., U.S. Government Printing Office, 1993, p 235-245